Development of an x-ray radiography platform to study laser-direct-drive energy coupling at the National Ignition Facility

L. Ceurvorst, W. Theobald, M. J. Rosenberg, et.al.

Development of an x-ray radiography platform to study laser-direct-drive energy coupling at the National Ignition Facility

L. Ceurvorst, W. Theobald, M. J. Rosenberg, et al.

COLLECTIONS

Paper published as part of the special topic on Proceedings of the 24th Topical Conference on High-Temperature Plasma Diagnostics

View Online   Export Citation   CrossMark

ARTICLES YOU MAY BE INTERESTED IN

The Vacuum Cherenkov Detector (VCD) for γ-ray measurements in inertial confinement fusion experiments
Review of Scientific Instruments **93**, 103543 (2022); https://doi.org/10.1063/5.0101830
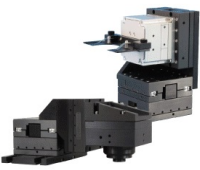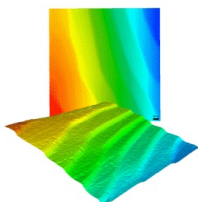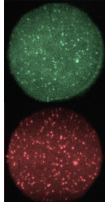
Development of a flat-field-response, four-channel x-ray imaging instrument for hotspot asymmetry studies
Review of Scientific Instruments **93**, 103545 (2022); https://doi.org/10.1063/5.0106990

Large area multi-filamentary plasma source for large volume plasma device–upgrade
Review of Scientific Instruments **93**, 103546 (2022); https://doi.org/10.1063/5.0095793

Review of Scientific Instruments

AIP Publishing

Development of an x-ray radiography platform to study laser-direct-drive energy coupling at the National Ignition Facility

L. Ceurvorst,[1,a] [ID] W. Theobald,[1,2] [ID] M. J. Rosenberg,[1] [ID] P. B. Radha,[1] [ID] C. Stoeckl,[1] [ID] R. Betti,[1,2]
K. S. Anderson,[1] [ID] J. A. Marozas,[1] [ID] V. N. Goncharov,[1,2] [ID] E. M. Campbell,[1] [ID] C. M. Shuldberg,[3] [ID]
R. W. Luo,[3] W. Sweet,[3] L. Aghaian,[3] L. Carlson,[3] B. Bachmann,[4] [ID] T. Döppner,[4] [ID] M. Hohenberger,[4] [ID]
K. Glize,[5] R. H. H. Scott,[5] [ID] A. Colaïtis,[6] [ID] and S. P. Regan[1,2] [ID]

AFFILIATIONS

[1] Laboratory for Laser Energetics, University of Rochester, Rochester, New York 14623-1299, USA
[2] Department of Mechanical Engineering, University of Rochester, Rochester, New York 14627, USA
[3] General Atomics, San Diego, California 92121, USA
[4] Lawrence Livermore National Laboratory, Livermore, California 94550, USA
[5] Central Laser Facility, STFC Rutherford Appleton Laboratory, Harwell Oxford, Oxfordshire, OX11 0QX, United Kingdom
[6] Centre Lasers Intenses et Applications, CELIA, Université de Bordeaux-CNRS-CEA, UMR 5107, Talence F-33405, France

Note: This paper is part of the Special Topic on Proceedings of the 24th Topical Conference
on High-Temperature Plasma Diagnostics.
[a] Author to whom correspondence should be addressed: lceurvorst@lle.rochester.edu

ABSTRACT

A platform has been developed to study laser-direct-drive energy coupling at the National Ignition Facility (NIF) using a plastic sphere target irradiated in a polar-direct-drive geometry to launch a spherically converging shock wave. To diagnose this system evolution, eight NIF laser beams are directed onto a curved Cu foil to generate He$_\alpha$ line emission at a photon energy of 8.4 keV. These x rays are collected by a 100-ps gated x-ray imager in the opposing port to produce temporally gated radiographs. The platform is capable of acquiring images during and after the laser drive launches the shock wave. A backlighter profile is fit to the radiographs, and the resulting transmission images are Abel inverted to infer radial density profiles of the shock front and to track its temporal evolution. The measurements provide experimental shock trajectories and radial density profiles that are compared to 2D radiation-hydrodynamic simulations using cross-beam energy transfer and nonlocal heat-transport models.

Published under an exclusive license by AIP Publishing. https://doi.org/10.1063/5.0098982

The coupling of laser energy to an imploding target in direct-drive inertial confinement fusion (ICF)[1] is a key parameter that determines the ablation pressure and the implosion velocity of the shell. According to current models, cross-beam energy transfer[2] is a major factor that limits the ablation pressure on National Ignition Facility (NIF)-scale targets, reducing the implosion velocity and shell kinetic energy. Hence, accurate measurements of the laser coupling efficiency for NIF-scale implosions are an important aspect of direct-drive ICF research.

A common method to obtain such measurements is x-ray radiography. This technique is broadly applied to a range of topics including hydrodynamic instabilities,[3–6] shock propagation,[7–10] and high-energy-density plasmas[11–13] and is well suited to diagnosing the density evolution of such systems. A platform was, therefore, developed at the NIF, which uses x-ray radiography and self-emission imaging[14] to monitor the trajectory of an imploding target and compares the results to state-of-the-art simulations.[15] Initially, this platform was designed to work with thin

(100-μm) plastic shell targets.[16] However, while the attenuation profiles inferred from the radiographs roughly matched the post-processed simulations, the self-emission images showed a significant reduction in ablation-front velocity compared to numerical predictions.[15] This was attributed to hydrodynamic instabilities such as laser imprint[17–19] and subsequent Rayleigh–Taylor growth,[20–22] significantly perturbing the target. Given the limited wavelength detuning capabilities and beam quality at the NIF, these instabilities are unavoidable with thin-shell targets. As a result, solid sphere targets were fielded to enable the quantification of energy coupling without these hydrodynamic challenges. Alongside this experimental optimization, a new technique for inferring the 2D density profiles of the targets from x-ray radiographs was developed. This paper presents the resulting platform for inferring energy coupling and radial density profiles in targets driven in polar direct drive (PDD) on the NIF.

Figure 1 shows the experimental configuration. A massive plastic (CH) spherical target with an outer diameter of 2.1 mm and density 1.07 g/cm^3 is placed at target chamber center (TCC) and driven by 184 NIF beams configured in a PDD geometry.[15] Experiments are then performed with 350–600 kJ of laser drive energy using a 7-ns ramp pulse. This profile reaches an intensity plateau at times between 3 and 5 ns depending on the peak intensity, maintaining intensity rise in the ramp in all cases. The maximum delivered laser intensity is varied between 4×10^{14} and 1.2×10^{15} W/cm^2. This launches a radial shock into the target, compressing and collapsing it inward. This compression is then monitored using time-gated x-ray radiography with a Cu backlighting foil located 5 mm away from the main target. The Cu foil is driven by eight laser beams delivering 59 kJ of energy over 7.75 ns, generating Cu He$_\alpha$ emission at ~8.4 keV.

These x rays pass through the target before being imaged by an array of 25-μm-diameter pinholes. The array is located 320 mm from TCC. The images are captured by a four-strip gated x-ray detector (GXD)[23] located along the target's equator with a nominal magnification of 2. An Au shield blocks the backlighter x-ray emission toward a second equatorial GXD, which records the x-ray flash from the shock collapsing in the center of the sphere.

Figure 2 shows raw radiography data for shot N210519-001. For this shot, 474 kJ of laser energy was delivered to the sphere with a maximum intensity of 8×10^{14} W/cm^2. The shocked material is visible in each sub-image, appearing as a ring of increased attenuation due to density compression. The strips were timed to capture data at $t = 5.1, 6.1, 7.1$, and 8.1 ns, and the pinhole array allowed four images to be captured per strip.

To infer the density profile from these radiographs, note that the optical depth of the target τ is given by

$$\tau = -\ln(T) = \int \rho(\vec{x})\mu(\vec{x})\mathrm{d}z, \tag{1}$$

where T is the transmission of the target, $\rho(\vec{x})$ and $\mu(\vec{x})$ are the density and opacity of the target at position $\vec{x}$, respectively, and z is the direction of propagation. In the case where ρ and μ are approximately spherically symmetric, the integral in Eq. (1) is simply an Abel transformation of $\rho \cdot \mu$. Thus, the radial density and opacity profile can be inferred by Abel inverting optical depth images of the target.

To obtain optical depth images, the backlighter profile must first be fit to the obtained radiographs. Typically, this is done by cropping each image and fitting only the portions of the backlighter unobscured by the target. However, as can be seen in Fig. 2, the target nearly eclipses the backlighter making such a fit unreliable, especially at early times. Instead, basic assumptions about the target and its
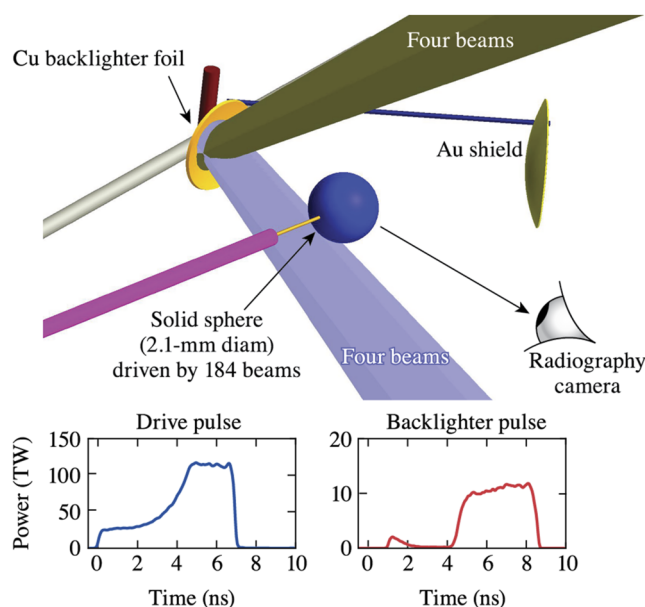

FIG. 1. Schematic of the solid-sphere laser-direct-drive energy coupling platform. The main target is shown in blue (center), the backlighter in yellow (left), and an Au shield in khaki (right). The radiography camera is located opposite to the backlighter. Example pulse shapes of the drive and backlighter beams are shown.
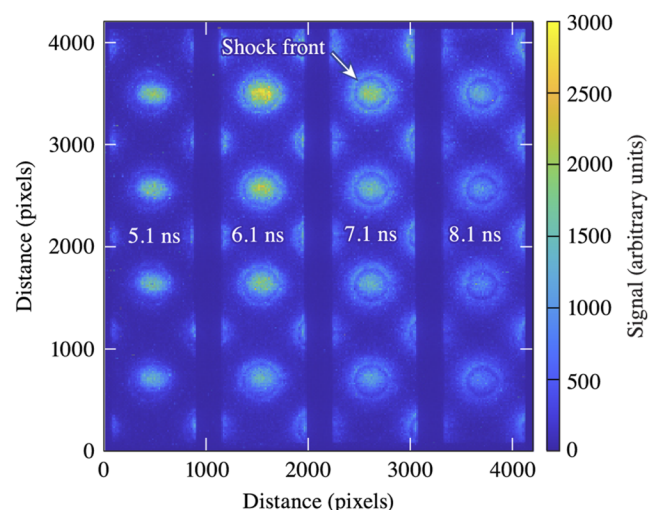

FIG. 2. Raw radiography data for shot N210519-01 using a maximum laser intensity of 8×10^{14} W/cm^2. In total, 16 images were captured on the four strips. The white numbers provide the timing of each strip.

resulting transmission profile must be made and incorporated into the overall fit.

The first assumption made is that the target remains roughly spherically symmetric and possesses two zones of differing densities and temperatures connected by linear attenuation transitions. A central unshocked sphere remains at its initial density, ρ_0 = 1.07 g/cm^3, and maintains a cold opacity of μ_0 = 3.2 cm^2/g. The attenuation then linearly rises until reaching a flat, compressed, hot region extending out to the ablation front. Its opacity and density are unknown, and as such, its attenuation will be included in the fit. Beyond the ablation front, the attenuation linearly falls to zero, representing the rapid drop in density and opacity caused by ablation.[10] Linear transitions were chosen because their Abel transformations can be analytically solved as shown in the supplementary material. However, because only the backlighter profile is kept in the final analysis, the final reconstructed profiles need not conform to this linearity.

Given the super-Gaussian profile of the beams driving the backlighter, the emission's spatial profile is assumed to be a superposition of two rotatable, elliptical super-Gaussians, one for each of the driving quads. The overall fit for a single image will then be this emission profile multiplied by the target's assumed transmission profile plus a constant background level.

The images within each strip are separated by about 60 ps due to the propagation of the gating pulse. At this time scale, no discernible hydrodynamic evolution is anticipated between images of the same strip. However, parallax reveals portions of the backlighter in some images that are concealed by the target in others. Thus, in order to maximize the amount of information available to each fit and to maintain consistency in the analysis, fits will be performed for entire strips at once rather than fitting each individual sub-image. The distance between backlighter and target images within a strip can be estimated from the metroligized pinhole separation, δ_P = 2.82 mm, and each object's magnification level. However, to account for alignment variance and to enable *in situ* measurements of the target and backlighter magnifications, these parameters are included in the fit, as is any rotation of the pinholes array.

Finally, the gain depletion, or "droop," must be accounted for.[24] As can be seen in Fig. 2, the bottom of the strips has significantly decreased signals. This well-known behavior is caused by conductor losses within the microchannel plate of the GXD.[25] To account for this, the droop is approximated as a linear function along the strip, the slope of which is included in and completes the final fit function. A full list of fitted equations is included in the supplementary material.

An example fit is shown in Fig. 3(b) after cropping in on a single sub-image. The fitted target and backlighter magnifications are 1.982 ± 0.005 and 1.954 ± 0.003, respectively, consistent with the expected magnifications within the positioning error of the pinhole array. Dividing the raw signal by the fitted profile yields the flat-field image. As shown in Fig. 3(c), the only visible structure beyond white noise in this image is the dark region on the right corresponding to the target stalk. The backlighter profile is then extracted from this fit and used to divide the raw data and produce the transmission image as shown in Fig. 3(d).

Abel inversion is highly sensitive to noise. To address this, the four images within each strip are correlated and averaged together to produce a single transmission profile at each time step. This
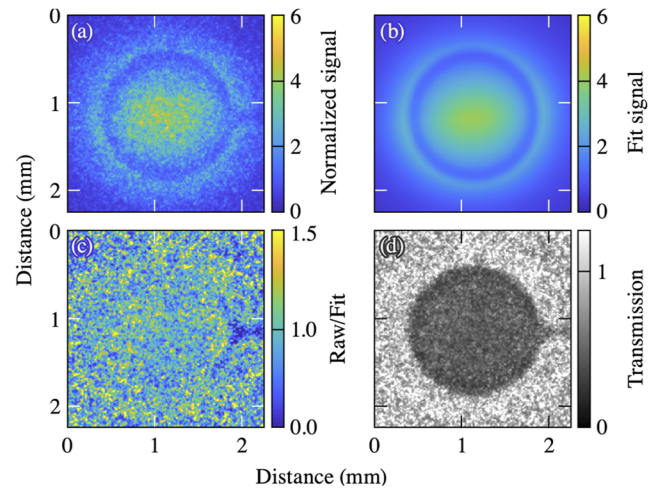

FIG. 3. Data analysis for a single image from shot N210519-001. (a) The raw image, (b) fitted function, (c) flat field, and (d) extracted transmission for a single sub-image at t = 7.1 ns. Calculations are performed on entire strips at once, but these figures are cropped to single images for ease of viewing.

introduces ~200 ps of additional temporal blurring but significantly improves the signal level. This is evident when comparing the composite image in Fig. 4(a) to Fig. 3(d). To convert these images to polar coordinates, an ellipse is fit to the composite profiles to find the target's center [Fig. 3(b)]. The transmission images are then converted to optical depth and unwrapped into the corresponding polar coordinates [Fig. 4(c)].

Radial optical depth lineouts are calculated by averaging the optical depth profile over a range of polar angles. The width of these
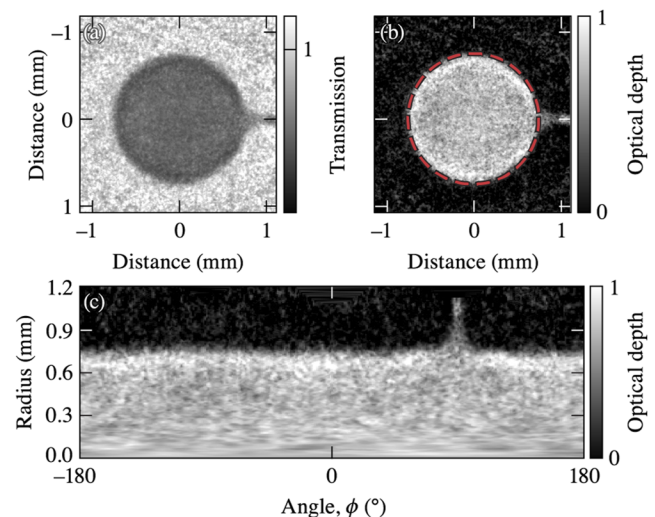

FIG. 4. Unwrapping to polar coordinates. (a) The composite transmission image at t = 7.1 ns. (b) The red dashed line superimposed on the optical depth image shows the elliptical fit used to determine the target's origin. (c) The optical depth image in polar coordinates. The perturbation at ϕ = 90° is the stalk.

ranges $\Delta\phi$ will be explored shortly, but for now will be kept at a full $\Delta\phi = 360°$ (excluding the region of the target stalk) to give the azimuthally averaged lineouts. These curves are then Abel inverted to give $\rho(r) \cdot \mu(r)$ at each time step.

Dividing these results by the cold opacity μ_0 gives a first approximation of the $\rho(r)$ profile. However, doing so results in lower densities in the shocked region than would be expected for a spherically converging shock[15] ($\rho_S \approx 3.8$ g/cm^3), and spherically integrating this profile reveals an unphysical loss of target mass ($> 20\%$). Thus, the assumption of a constant opacity is not valid for this set of data. Instead, the material beyond the shock front has been sufficiently heated and ionized to reduce its overall opacity.[8,26] To approximate this, a step function will be used where the cold opacity is applied to the unshocked material and a reduced hot opacity is applied beyond the shock front so that the total mass of the target follows theoretical predictions.

The mass of the target as a function of time is taken from simulations performed using the *DRACO* 2D hydrocode,[27] which included cross-beam-energy-transfer and nonlinear heat-transport models. These simulations sought to model the observed energy coupling of these experiments. Their details will be discussed in a forthcoming manuscript analyzing the scientific results of these experiments. The total mass was then calculated from these simulations, showing a decrease from 0.50 mg at $t = 5.1$ ns to 0.48 mg at $t = 8.1$ ns as the material was ablated from the target's surface.

Matching the experiment's total mass to the simulated masses, the hot opacity was calculated to be $\mu_{\text{hot}} = 2.5 \pm 0.2$ cm^2/g. The stepped opacity profile was then used to produce the final inferred density profiles shown in Fig. 5. The results are much more consistent with the simulated density profiles. Note that the simulations

were blurred by 31 μm to match the imaging system's response function in this plot.

It is important to note that this method of conserving mass significantly reduces the inferred density profiles' dependence on the assumed cold opacity. In the fit, the interior region is assumed to have fixed opacity and density. Since this interior region is much larger than the surrounding compressed region at these early times, these parameters largely determine the amplitude of the backlighter when the fit is performed. In practice, this causes features in the $\rho \cdot \mu$ profile to be stretched about $\rho_0\mu_0$ as μ_0 is varied. However, beyond noise, the only feature that deviates from $\rho_0\mu_0$ is the shocked region, and its density is now altered to conserve mass. As a result, the dependence on the assumed opacity is minimized, and the inferred density profiles are robust.

This same technique can be applied to generate a 2D density map by reducing the angular bin width, $\Delta\phi$. Doing so yields the average density profile within spherical wedges of the target. A full 2D image can then be created by plotting these profiles along their bins' central angles and interpolating in polar coordinates.

To validate this technique, the 2D simulation results were post-processed using *Spect3D*[28] to calculate transmission images including the instrument response function, and the above algorithm was applied starting from the unwrapping of the optical depth images to polar coordinates with $\Delta\phi = 45°$. As shown in Fig. 6, the resulting reconstructed density profiles almost exactly match the simulated profiles when blurred with the instrument response function. This yields a root-mean-square error (RMSE) between the reconstruction and the blurred density profile of just 0.06 g/cm^3. The largest deviations occur at large density gradients and are likely due to the Abel inversion method used here.[29]

Note that such a low RMSE was attainable due to the lack of noise in the artificial images. In the experiment, the quality of the
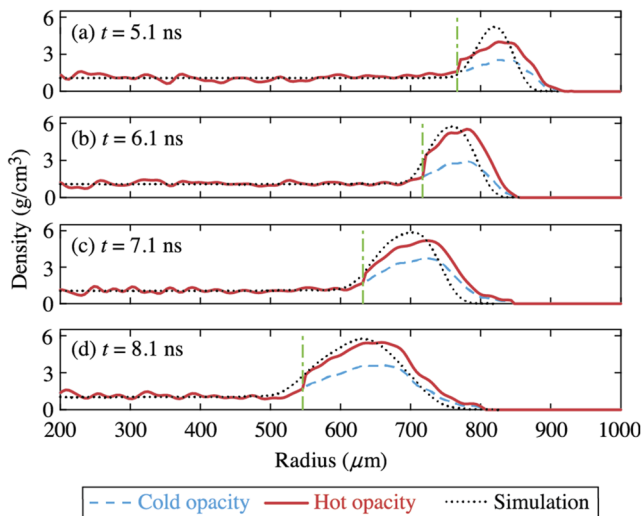

FIG. 5. Inferred azimuthally averaged density profiles. The initial density calculation using only cold opacity (dashed blue) and the mass-conserving calculation using a stepped opacity profile (solid red) are compared to the blurred simulated density profile (dotted black) at (a) 5.1, (b) 6.1, (c) 7.1, and (d) 8.1 ns. Vertical lines (dashed-dotted green) indicate the shock position beyond which the calculated hot opacity was applied.
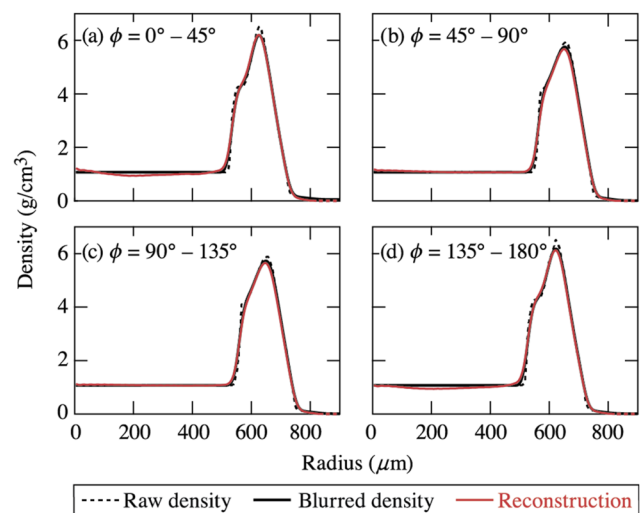

FIG. 6. Reconstructed density profiles (red) are calculated from simulated transmission images binned at (a) 0°–45°, (b) 45°–90°, (c) 90°–135°, and (d) 135°–180° and compared to the high-resolution (dotted black) and blurred (solid black) simulated density profiles.

reconstruction degrades due to the presence of noise. For instance, the unshocked regions should have remained at a constant value of 1.07 g/cm^3 but varied with an RMSE of 0.4 g/cm^3 using $\Delta\phi = 45°$. To reduce this variation, larger values of $\Delta\phi$ must be used, reducing the RMSE as low as 0.2 g/cm^3 but allowing only low-mode asymmetries to be captured with this method. Alternatively, a more robust Abel inversion model[30] than the one fielded here might further reduce the reconstruction's noise dependence. Nonetheless, general trends can still be extracted from these data, which will be explored in a future manuscript presenting the analysis of the full campaign.

In summary, a method of inferring 2D density profiles from x-ray radiographs of a spherically quasi-symmetric system has been presented. This technique was developed for interpreting solid-sphere implosions but can be generalized to other systems by altering the initial fit's transmission function. When applied to artificial radiographs, this technique was able to reproduce simulated profiles with extreme accuracy. The results of this analysis are being applied to constrain models of energy coupling in NIF PDD experiments. Future work will focus on the effects of a non-monochromatic backlighter and the implementation of more robust Abel inversion techniques.

See the supplementary material for a derivation of the functions used in the initial fit.

AUTHOR DECLARATIONS

Conflict of Interest

The authors have no conflicts to disclose.

Author Contributions

L. Ceurvorst: Formal analysis (equal); Writing – original draft (equal). **W. Theobald**: Conceptualization (equal); Investigation (equal); Supervision (equal). **M. J. Rosenberg**: Investigation (equal); Project administration (equal). **P. B. Radha**: Conceptualization (equal); Investigation (equal); Validation (equal). **C. Stoeckl**: Methodology (equal). **R. Betti**: Conceptualization (equal); Supervision (equal). **K. S. Anderson**: Investigation (equal); Supervision (equal). **J. A. Marozas**: Methodology (equal). **V. N. Goncharov**: Methodology (equal); Supervision (equal). **E. M. Campbell**: Project administration (equal); Supervision (equal). **C. M. Shuldberg**: Resources (equal). **R. W. Luo**: Resources (equal). **W. Sweet**: Resources (equal). **L. Aghaian**: Resources (equal). **L. Carlson**: Resources (equal). **B. Bachmann**: Investigation (equal); Resources (equal). **T. Döppner**: Investigation (equal); Resources (equal). **M. Hohenberger**: Conceptualization (equal); Investigation (equal); Resources (equal). **K. Glize**: Investigation (equal). **R. H. H. Scott**: Investigation (equal). **A. Colaïtis**: Investigation (equal). **S. P. Regan**: Project administration (equal); Supervision (equal).

DATA AVAILABILITY

Raw data were generated at the National Ignition Facility. Derived data supporting the findings of this study are available from the corresponding author upon reasonable request.

REFERENCES

[1] R. S. Craxton et al., Phys. Plasmas **22**, 110501 (2015).
[2] I. V. Igumenshchev et al., Phys. Plasmas **17**, 122708 (2010).
[3] V. A. Smalyuk, T. R. Boehly, D. K. Bradley, J. P. Knauer, and D. D. Meyerhofer, Rev. Sci. Instrum. **70**, 647 (1999).
[4] O. Sadot et al., Phys. Rev. Lett. **95**, 265001 (2005).
[5] L. Ceurvorst et al., High Energy Density Phys. **37**, 100851 (2020).
[6] M. Karasik et al., Phys. Plasmas **28**, 032710 (2021).
[7] L. Antonelli et al., Phys. Rev. E **95**, 063205 (2017).
[8] D. C. Swift et al., Rev. Sci. Instrum. **89**, 053505 (2018).
[9] C. Mailliet et al., Phys. Plasmas **26**, 082703 (2019).
[10] D. C. Swift et al., Rev. Sci. Instrum. **92**, 063514 (2021).
[11] H.-S. Park et al., Phys. Plasmas **15**, 072705 (2008).
[12] A. Morace et al., Phys. Plasmas **21**, 102712 (2014).
[13] A. G. MacPhee et al., Phys. Rev. E **95**, 031204 (2017).
[14] D. T. Michel et al., Rev. Sci. Instrum. **83**, 10E530 (2012).
[15] P. B. Radha et al., Phys. Plasmas **23**, 056305 (2016).
[16] M. Hohenberger et al., Phys. Plasmas **22**, 056308 (2015).
[17] V. N. Goncharov et al., Phys. Plasmas **7**, 2062 (2000).
[18] S. X. Hu et al., Phys. Plasmas **23**, 102701 (2016).
[19] L. Ceurvorst et al., Phys. Rev. E **101**, 063207 (2020).
[20] Lord Rayleigh, Proc. London Math. Soc. **XIV**, 170 (1883).
[21] A. Casner et al., Phys. Plasmas **22**, 056302 (2015).
[22] D. A. Martinez et al., Phys. Rev. Lett. **114**, 215004 (2015).
[23] J. A. Oertel et al., Rev. Sci. Instrum. **77**, 10E308 (2006).
[24] M. Koga and H. Shiraga, Rev. Sci. Instrum. **88**, 083514 (2017).
[25] J. A. Oertel and T. N. Archuleta, Rev. Sci. Instrum. **85**, 11D622 (2014).
[26] S. X. Hu, L. A. Collins, J. P. Colgan, V. N. Goncharov, and D. P. Kilcrease, Phys. Rev. B **96**, 144203 (2017).
[27] P. B. Radha et al., Phys. Plasmas **12**, 032702 (2005).
[28] J. J. MacFarlane, I. E. Golovkin, P. Wang, P. R. Woodruff, and N. A. Pereyra, High Energy Density Phys. **3**, 181 (2007).
[29] G. Pretzier, Z. Naturforsch., A: Phys. Sci. **46**, 639 (1991).
[30] P. S. Kolhe and A. K. Agrawal, Appl. Opt. **48**, 3894 (2009).